

CLASSES OF REACTIONS

- ELASTIC SCATTERING

$$A=B, a=b$$

No change of internal states

$$\therefore Q=0$$

- "Size" of nuclei
- Range of nuclear force

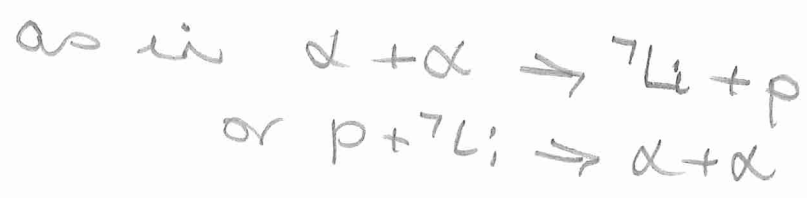
- INELASTIC SCATTERING

(usually means) $a=b$ and $B=A^*$

- Energy state structure of A

- Rearrangement collisions

$$a \neq b \text{ and } A \neq B$$



- Capture reactions



MAY SUBDIVIDE ABOVE TWO

- Compound nucleus
- Direct stripping
- Direct knockout

(Satchler Fig 2.28
2.29)

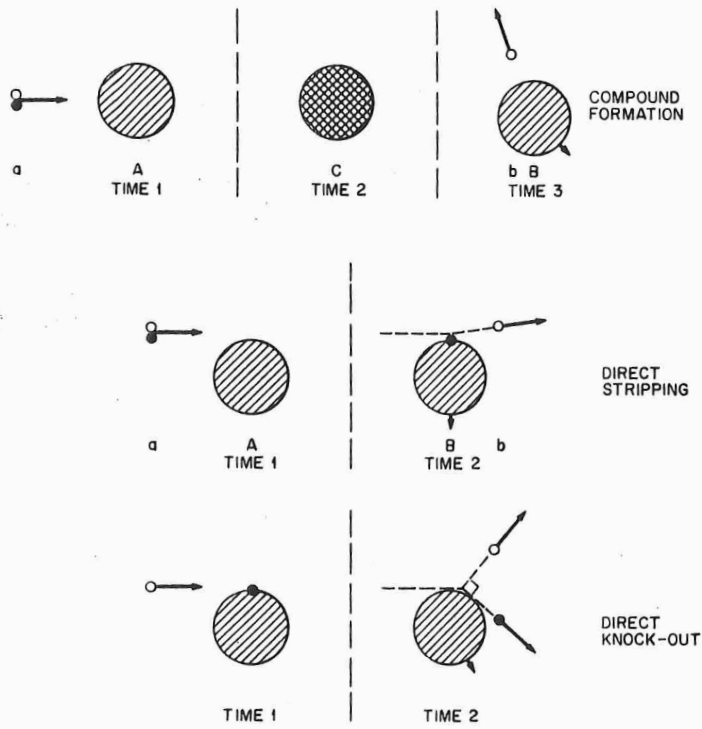


Figure 2.28 Illustrating schematically the two limiting kinds of nuclear reaction, compound nucleus formation and decay, and direct reactions. The latter are represented by stripping and knock-out occurring in the nuclear surface

Satchler
Intro. to Nuclear
Reactions

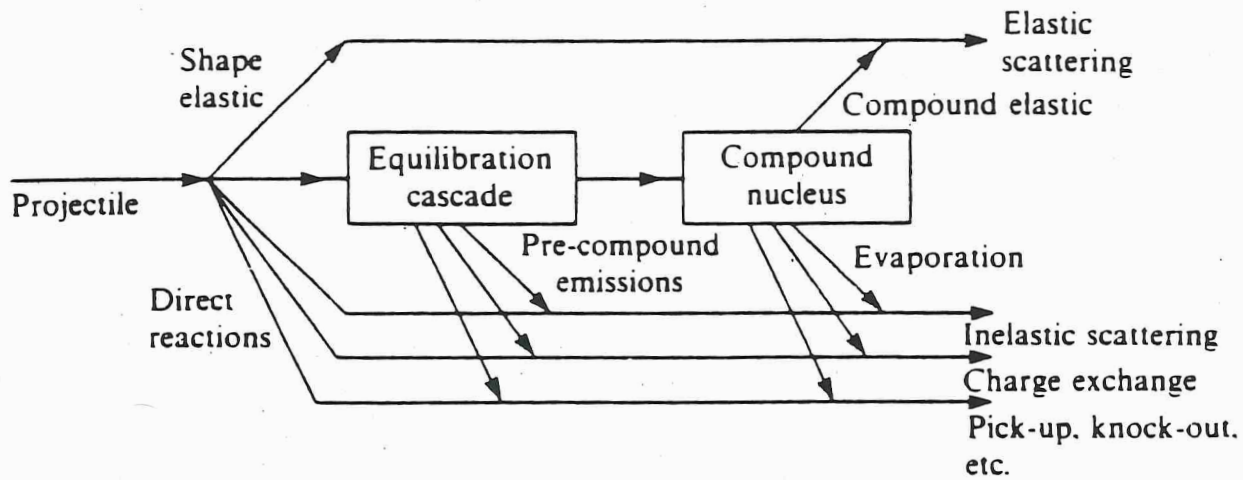


Fig. 19.5 Direct, pre-compound and compound nucleus contributions to a nuclear reaction.

sections and all the other non-elastic reactions. This shows the connections between the different reaction mechanisms.

• COULOMB BARRIER

— tunneling at low energy (CAULDRONS Fig 4.2)
 $\sigma \ll \pi R_{A+a}^2$

→ high energy > Coulomb barrier

$$\sigma \sim \pi R_{A+a}^2$$

$\lesssim 1 \text{ GeV}$ {

• Fragmentation reactions
($A \sim$ medium)

• Collision-induced fission
($A \sim$ heavy)

• Spallation is fragmentation by
p, d, or n

$\gtrsim 1 \text{ GeV}$

Collisions \rightarrow pions, other hadrons
(cosmic rays in Earth's atmosphere)

$\gtrsim 100 \text{ GeV}$

\rightarrow quark-gluon plasma
(Big bang, neutron stars)

PHOTONS

- Rayleigh scattering from atoms
- Photoelectric absorption



- Compton scattering on atomic electrons

- Pair production



(Bas Fig 5.12)

with threshold $2m_e c^2$ ($\approx 1.02 \text{ MeV}$)

- Photodissociation

(Bas Fig 3.8)

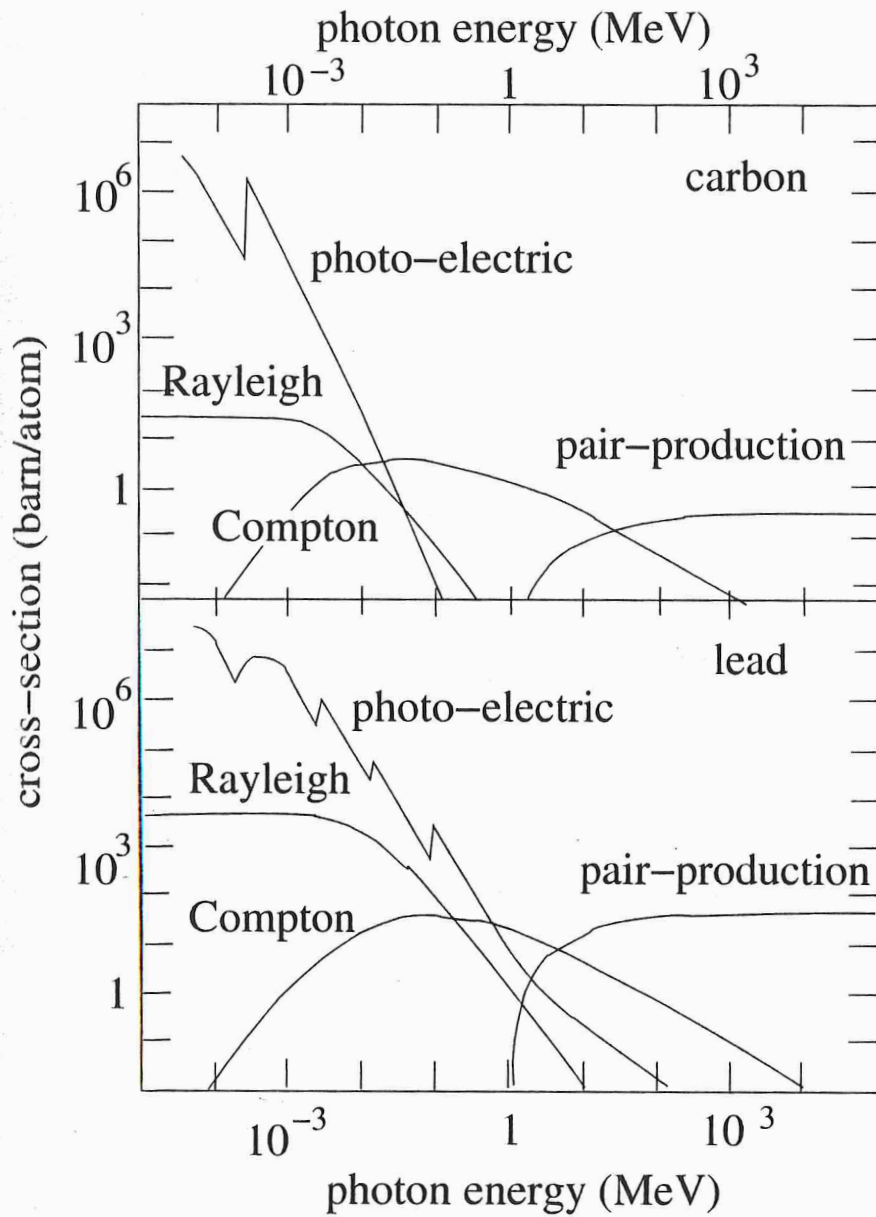


Fig. 5.12. Photon cross-sections on carbon and lead [1] as explained in the text. At low energy, $1 \text{ keV} < E < 100 \text{ keV}$, photo-electric absorption dominates while electron-positron pair production dominates for $E \gg 2m_e c^2$. Compton scattering dominates at intermediate energies. Photo-nuclear absorption (Fig. 3.8) is of minor importance.

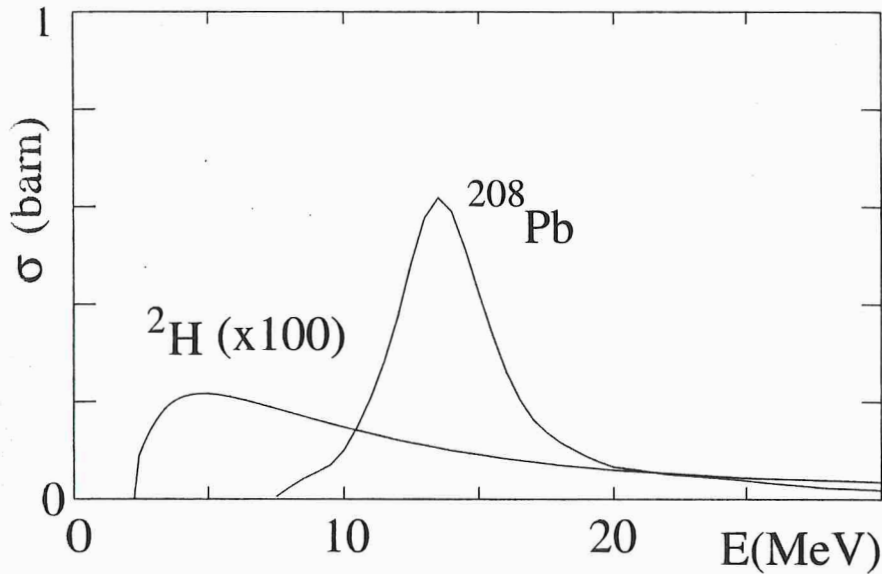


Fig. 3.8. The cross-sections for photo-dissociation of ${}^2\text{H}$ and of ${}^{208}\text{Pb}$ [30]. The cross-section of Pb exhibits a *giant resonance* typical of heavy nuclei.

Neutrinos Methods for calculating neutrino cross-sections will be presented in Sects. 3.2 and 3.4. Since neutrinos are subject to only weak interactions, their cross sections are considerably smaller than those of other particles. For neutrino energies much less than the masses of the intermediate vector bosons, $m_W c^2 = 80.4 \text{ GeV}$ and $m_Z c^2 = 91.2 \text{ GeV}$ the cross-sections are proportional to the square of the Fermi constant

$$\frac{G_F^2}{(\hbar c)^4} = 5.297 \times 10^{-48} \text{ m}^2 \text{ MeV}^{-2} \quad (3.36)$$

By dimensional analysis, this quantity must be multiplied by the square of an energy to make a cross-section. The cross-sections for several neutrino induced reactions are given in Table 3.1. For nuclear physics, neutrinos of energy $E_\nu \sim 1 \text{ MeV}$ are typical so, multiplying (3.36) by 1 MeV^2 , gives cross-sections of order 10^{-48} m^2 .

REACTIONS - direct capture



$S(E) \approx \text{constant}$

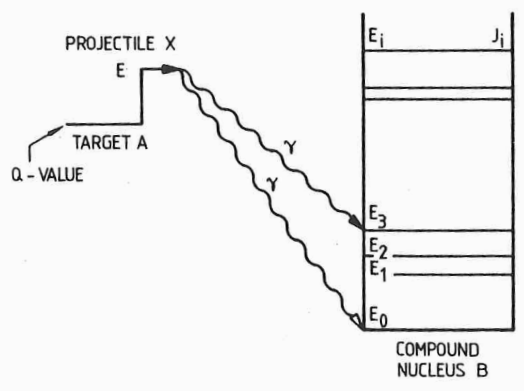
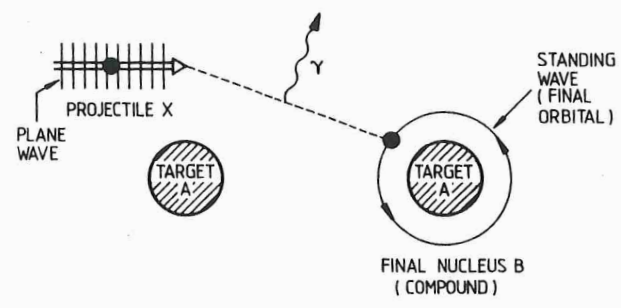


FIGURE 4.9. Illustrated is a capture reaction $A(x, \gamma)B$, where the entrance channel $A + x$ goes directly to states in the final compound nucleus B with the emission of γ -radiation. This process is called a direct-capture reaction and can occur for all energies E of the projectile.

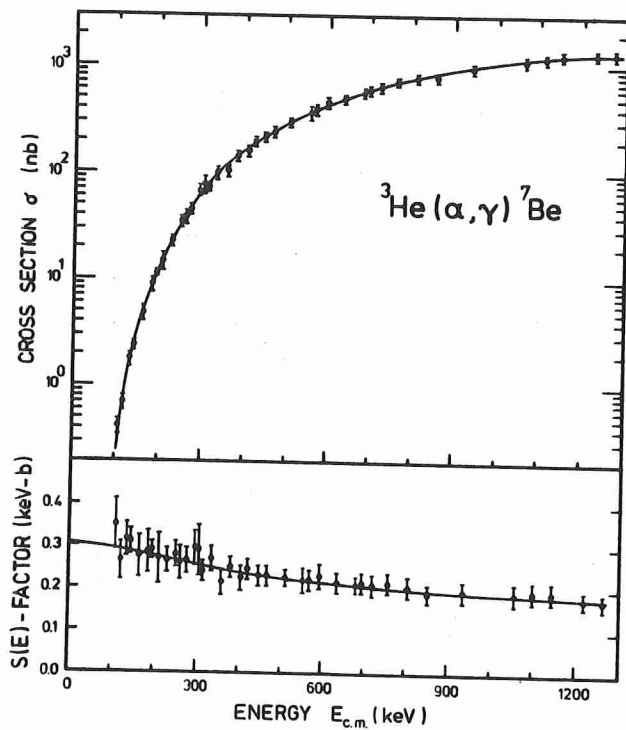
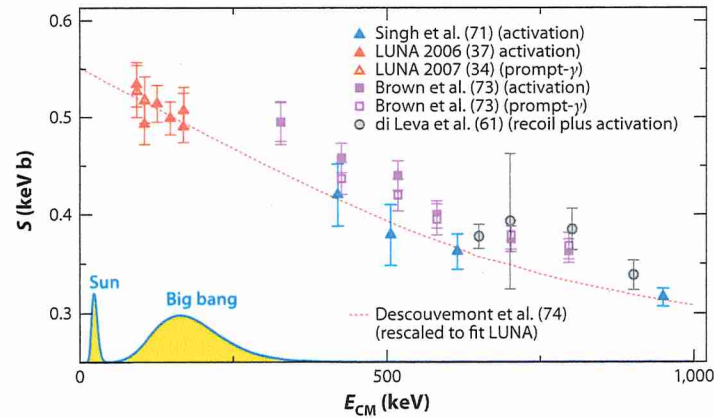
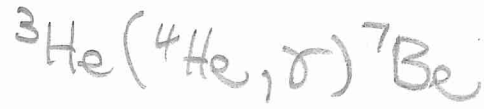


FIGURE 4.4. Energy dependence of the cross section $\sigma(E)$ and the factor $S(E)$ for the ${}^3\text{He}(\alpha, \gamma){}^7\text{Be}$ reaction (Krä82). The line through the data points represents a theoretical description of the cross section in terms of the direct-capture model. This theory is used to extrapolate the data to zero energy. Data from other sources (chap. 6) give a higher absolute scale (40% difference).



AR Brogini C, et al. 2010.
Annu. Rev. Nucl. Part. Sci. 60:53–73

- Key to ${}^7\text{Be}$ and ${}^8\text{Be}$ solar ν 's
- Key to ${}^7\text{Li}$ synthesis by Big Bang

REACTIONS with narrow & isolated resonances

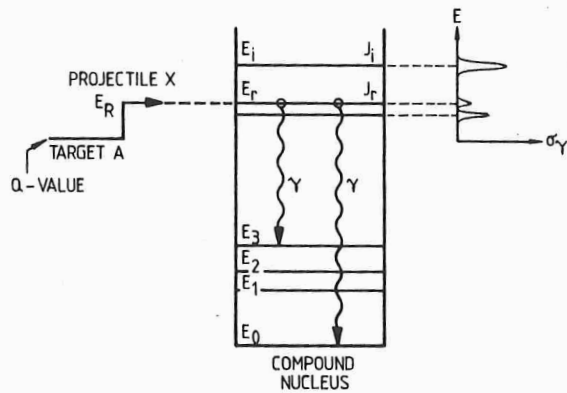
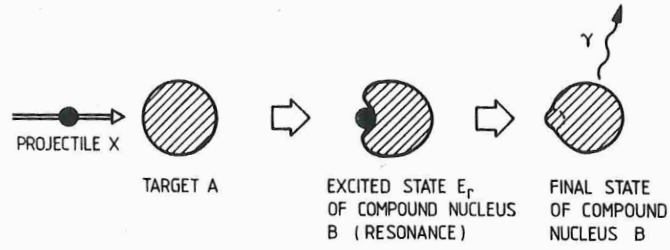


FIGURE 4.10. Illustrated is a capture reaction $A(x, \gamma)B$, where the entrance channel $A + x$ forms an excited state E_r in the compound nucleus B at an incident energy of E_r . The excited state E_r decays into lower-lying states with the emission of γ -radiation. This process is called a resonant capture reaction and can occur only at selected energies where $Q + E_r$ matches E_r . At these resonant energies E_r , the capture cross section σ may exhibit large maxima.

A SINGLE (OR ISOLATED) RESONANCE

- Wavefunctions of particle outside and inside the nucleus must match at the surface

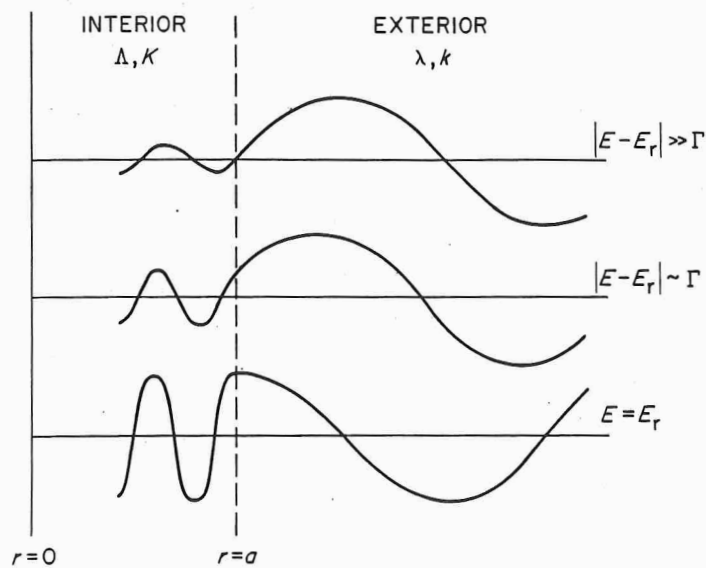


Figure 4.35 Illustrating the wave function for a neutron outside and just inside the surface ($r = a$) of a nucleus on, near and far from a resonance. For clarity the internal and external wavelengths are shown much more nearly equal than is usually the case; in practice, $\lambda \gg \Delta$ so that the interior amplitude when off-resonance is much smaller than shown here

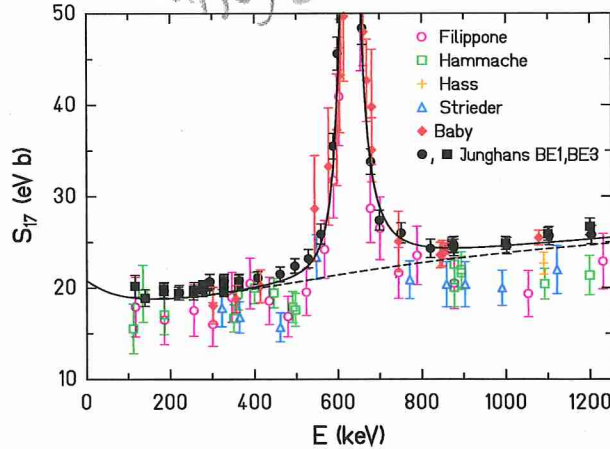


FIG. 9 (color online). $S_{17}(E)$ vs center-of-mass energy E , for $E \leq 1250$ keV. Data points are shown with total errors, including systematic errors. Dashed line: scaled Descouvemont (2004) curve with $S_{17}(0) = 20.8$ eV b; solid line: including a fitted 1^+ resonance shape.

in Solar Fusion I. Total errors, including systematic errors, are shown on each data point, to facilitate a meaningful comparison of different data sets. All data sets exhibit a similar $S_{17}(E)$ energy dependence, indicating that they differ mainly in absolute normalization.

Following the discussion in Sec. IX.B, we determine our best estimate of $S_{17}(0)$ by extrapolating the data using the scaled theory of Descouvemont (2004) (Minnesota calculation). We performed two sets of fits, one to data below the resonance, with $E \leq 475$ keV, where we felt the resonance contribution could be neglected. In this region, all the individual $S_{17}(0)$ error bars overlap, except for the Bochum result, which lies low.

We also made a fit to data with $E \leq 1250$ keV, where the 1^+ resonance tail contributions had to be subtracted. We did this using the resonance parameters of Junghans *et al.* (2003) ($E_p = 720$ keV, $\Gamma_p = 35.7$ keV, and $\Gamma_\gamma = 25.3$ meV), adding in quadrature to data errors an error of 20% of the resonance subtraction. In order to minimize the error induced by variations in energy averaging between experiments, we excluded data close to the resonance, from 490 to 805 keV,

where the S factor is strongly varying and the induced error is larger than 1.0 eV b. Above the resonance, the data have smaller errors. Only the Filippone *et al.* (1983) and Weizmann group error bars overlap the UW–Seattle/TRIUMF error bars.

Figure 9 shows the best-fit Descouvemont (2004) (Minnesota interaction) curve from the $E \leq 475$ keV fit [together with the 1^+ resonance shape determined by Junghans *et al.* (2003), shown here for display purposes]. Our fit results are shown in Table VII. The errors quoted include the inflation factors, calculated as described in the Appendix. The main effect of including the inflation factors is to increase the error on the combined result by the factor 1.7 for $E \leq 475$ keV, and by 2.0 for $E \leq 1250$ keV. Both the $S_{17}(0)$ central values and uncertainties from the combined fits for these two energy ranges agree well, the latter because the added statistical precision in the $E \leq 1250$ keV fit is mostly offset by the larger inflation factor.

We also did fits in which the low-energy cutoff was varied from 375 to 475 keV and the high-energy exclusion region was varied from 425–530 to 805–850 keV. The central value of $S_{17}(0)$ changed by at most 0.1 eV b. On this basis we assigned an additional systematic error of ± 0.1 eV b to the results for each fit region.

To estimate the theoretical uncertainty arising from our choice of the nuclear model, we also performed fits using the shapes from other plausible models: Descouvemont (2004) plus and minus the theoretical uncertainty shown in Fig. 8 of that paper; Descouvemont and Baye (1994); the CD-Bonn 2000 calculation shown in Fig. 15 of Navrátil *et al.* (2006b); and four potential-model calculations fixed alternately to reproduce the ${}^7\text{Li} + n$ scattering lengths, the best-fit ${}^7\text{Be} + p$ scattering lengths, and their upper and lower limits (Davids and Typel, 2003). The combined-fit results for all these curves, including Descouvemont (2004), are shown in Table VIII.

We estimate the theoretical uncertainty on $S_{17}(0)$ from the spread of results in Table VIII: ± 1.4 eV b for the $E \leq 475$ keV fits, and ${}^{+1.5}_{-0.6}$ eV b from the $E \leq 1250$ keV fits (the smaller error estimate in the latter case reflects the exclusion of the poorer potential-model fits). We note that the estimated uncertainties are substantially larger than those given by Junghans *et al.* (2003) and by Descouvemont (2004).

TABLE VII. Experimental $S_{17}(0)$ values and (inflated) uncertainties in eV b, and χ^2/dof determined by fitting the Descouvemont (2004) Minnesota calculation to data with $E \leq 475$ keV and with $E \leq 1250$ keV, omitting data near the resonance in the latter case.

Fit range Experiment	$E \leq 475$ keV			$E \leq 1250$ keV		
	$S_{17}(0)$	σ	χ^2/dof	$S_{17}(0)$	σ	χ^2/dof
Baby	20.2	1.4 ^a	0.5/2	20.6	0.5 ^a	5.2/7
Filippone	19.4	2.4	4.7/6	18.0	2.2	15.8/10
Hammache	19.3	1.1	4.8/6	18.2	1.0	12.5/12
Hass				18.9	1.0	0/0
Junghans BE3	21.6	0.5	7.4/12	21.5	0.5	12.3/17
Strieder	17.2	1.7	3.5/2	17.1	1.5	5.1/6
Mean	20.8	0.7	9.1/4	20.3	0.7	18.1/5

^aWe include an additional 5% target damage error on the lowest three points, consistent with the total error given in the text by Baby *et al.* (2003a) [M. Hass, 2009 (private communication)].

Breit-Wigner formula

$$\sigma(E) = \pi \lambda^2 \frac{(2J+1)}{(2J_1+1)(2J_2+1)} (1+\delta_{l2}) \frac{\Gamma_a \Gamma_b}{(E-E_r)^2 + (\Gamma/2)^2}$$

$$\pi \lambda^2 = \frac{656.6}{\sqrt{E_{keV}}} b$$

J_1 = spin of projectile

J_2 = spin of target

Γ_a = width of formation state in compound nucleus

Γ_b = width of final state

$$\langle \sigma v \rangle = \left(\frac{2\pi}{\mu kT} \right)^{3/2} k^2 (w\gamma)_k \exp\left(-\frac{E_r}{kT}\right)$$

$$(w\gamma) = \omega \frac{\Gamma_a \Gamma_b}{\Gamma}$$

$$\Gamma = \Gamma_a + \Gamma_b + \dots$$

$$\omega = \frac{(2J+1)}{(2J_1+1)(2J_2+1)}$$

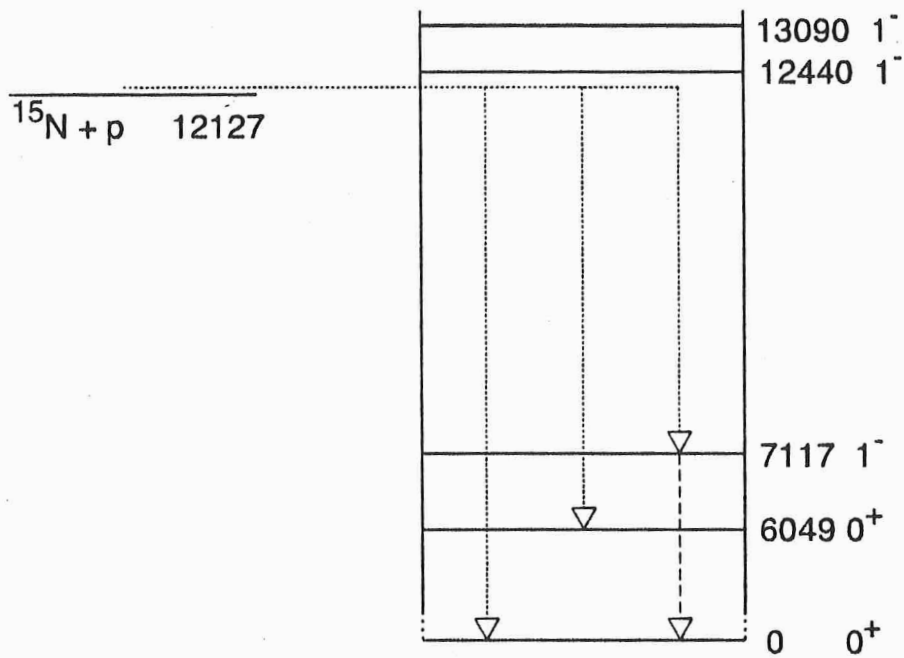


Figure 1. Energy levels of ^{16}O relevant to the $^{15}\text{N}(p,\gamma)^{16}\text{O}$ reaction at low energy. Primary (dotted) and secondary (dashed) γ -ray transitions are also shown.

W (GV)

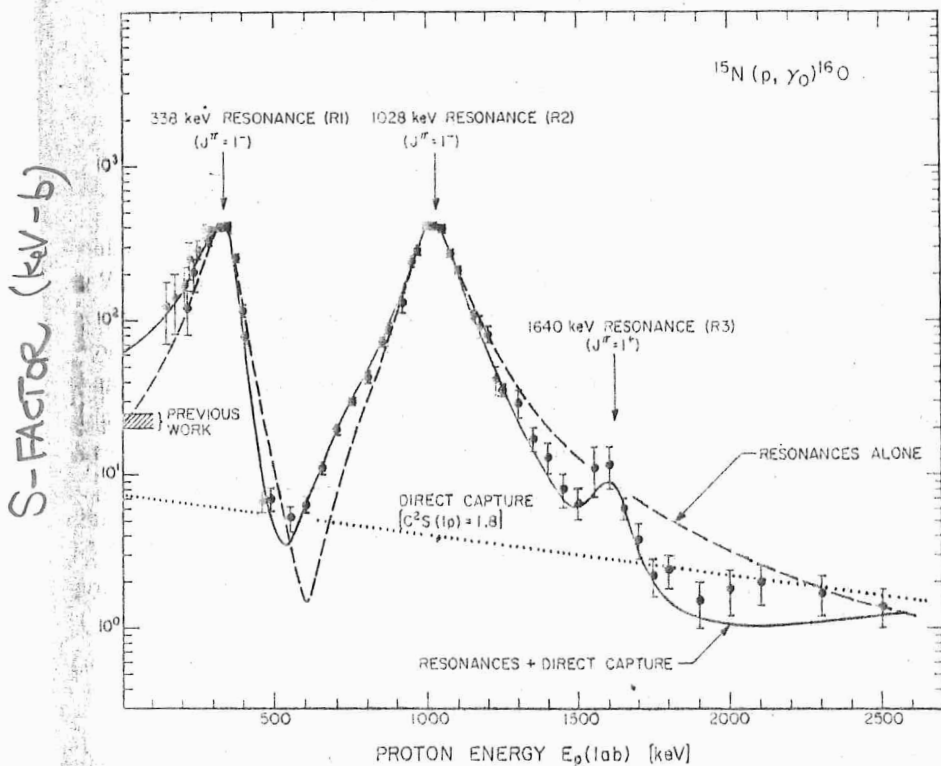


Fig. 3. Astrophysical S -factor for the reaction $^{15}\text{N}(p, \gamma)^{16}\text{O}$. The dashed line through the data points represents the results from an analysis solely in terms of the two $J^\pi = 1^-$ resonances revealing a S -factor of $S(0) = 22 \text{ keV} \cdot \text{b}$. The solid line represents the results from an analysis including in addition a direct-capture component (dotted line) in the capture process. This analysis reveals an extrapolated S -factor of $S(0) = 64 \pm 6 \text{ keV} \cdot \text{b}$. The sharp resonance at $E_p = 429 \text{ keV}$ (fig. 2) does not contribute significantly to the burning process.

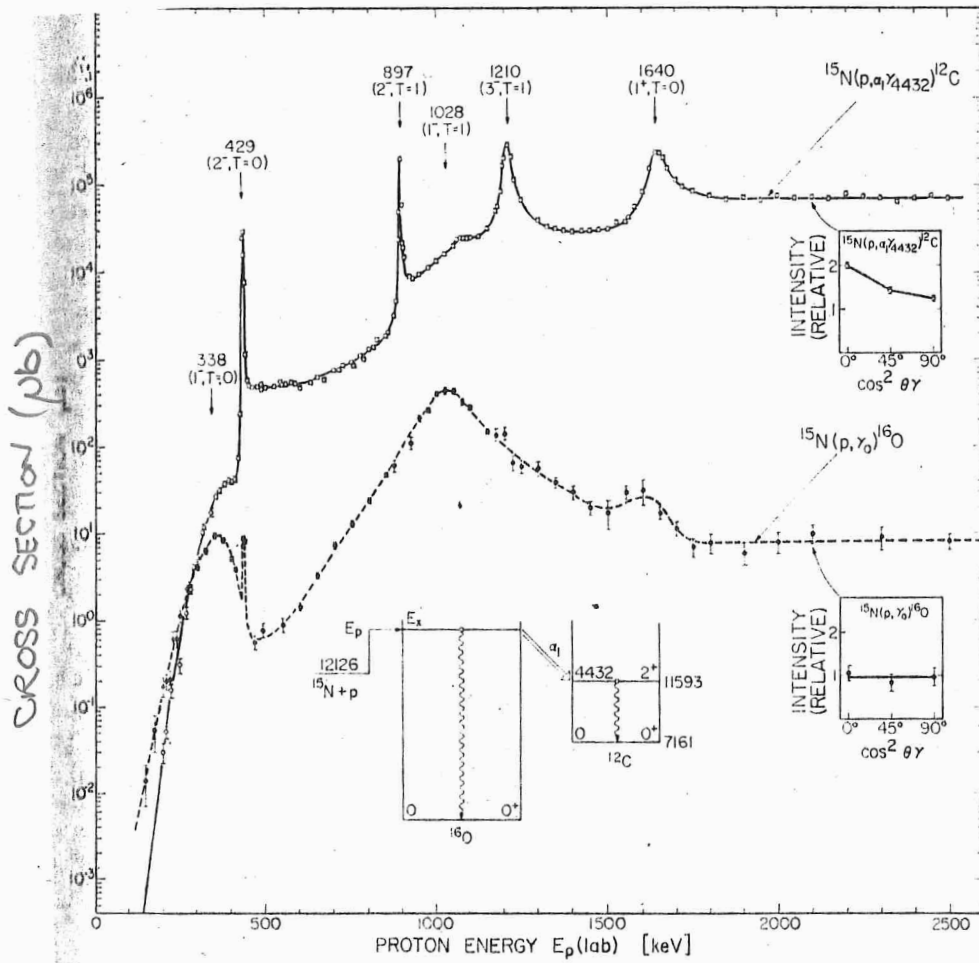


Fig. 2. Total cross sections for the $^{15}\text{N}(p, \alpha_1 \gamma_1)^{12}\text{C}$ and $^{15}\text{N}(p, \gamma_0)^{16}\text{O}$ reactions are shown as a function of beam energy. The solid and dashed lines through the data points are placed to guide the eye. The insets show the γ -ray angular distributions observed at $E_p = 2.10$ MeV.

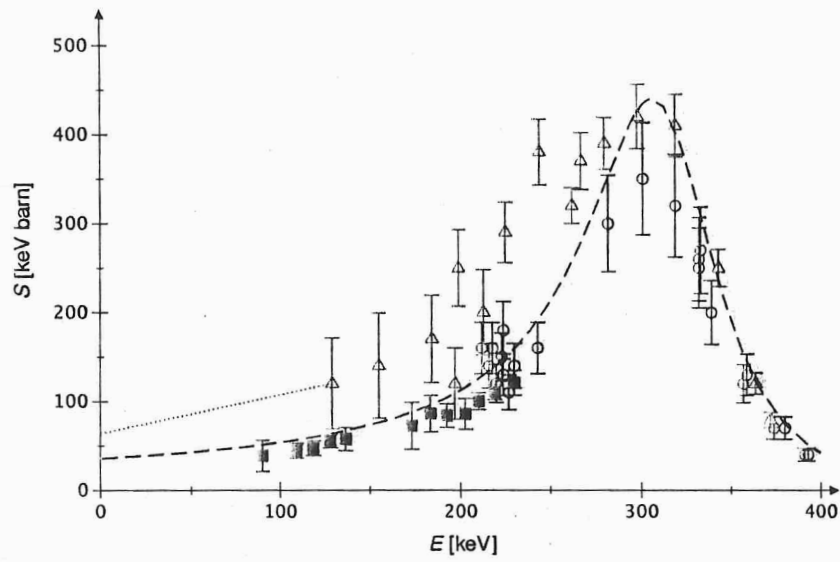


Figure 4. The $^{15}\text{N}(p,\gamma)^{16}\text{O}$ astrophysical S -factor. Experimental data from [5] (blue circles, limited to $E \geq 210$ keV), [6] (green triangles) and the present work (red-filled squares). Error bars reflect statistical and systematic uncertainties summed in quadrature. Dotted line, previous low-energy extrapolation by the NACRE compilation [8]. Dashed line, previous R-matrix fit and shaded area, its quoted 17% uncertainty [9].

REACTIONS - with broad resonances

- take account of energy spread
- see Coulombs

made

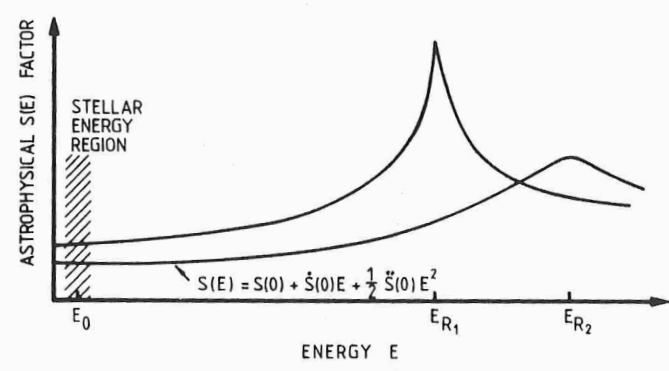
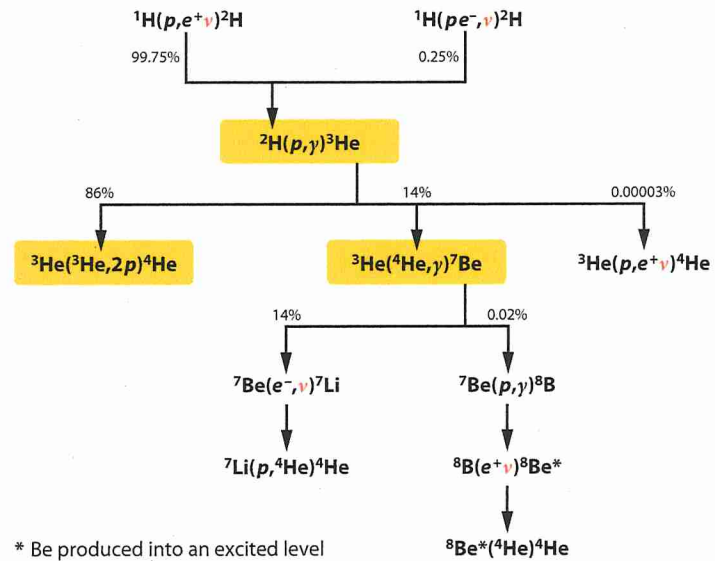

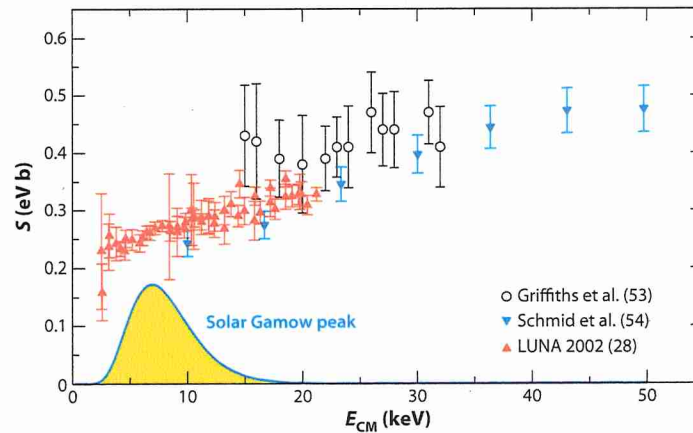


FIGURE 4.15. Energy dependence of the $S(E)$ factor for two broad resonances with maxima at energies E_{R1} and E_{R2} . The stellar energy region is also indicated, where E_0 refers to the Gamow energy.



 Brogini C, et al. 2010.
 Annu. Rev. Nucl. Part. Sci. 60:53–73



AR Brogini C, et al. 2010.
Annu. Rev. Nucl. Part. Sci. 60:53–73

- Deuterium burning in protostars
- One step in ${}^3\text{He}$ synthesis in low mass main sequence stars
- Key to breaking D bottleneck in Big Bang nucleosynthesis

Annual Reviews

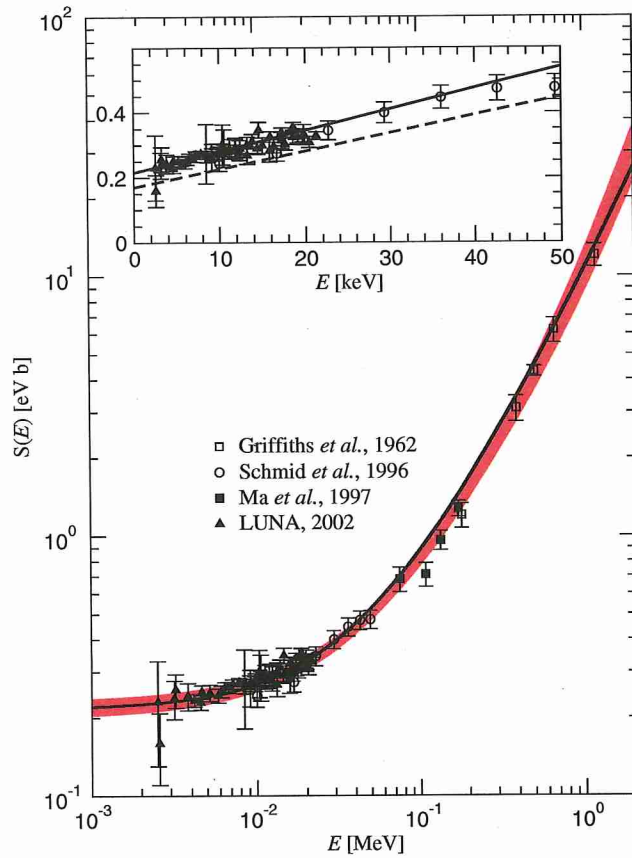
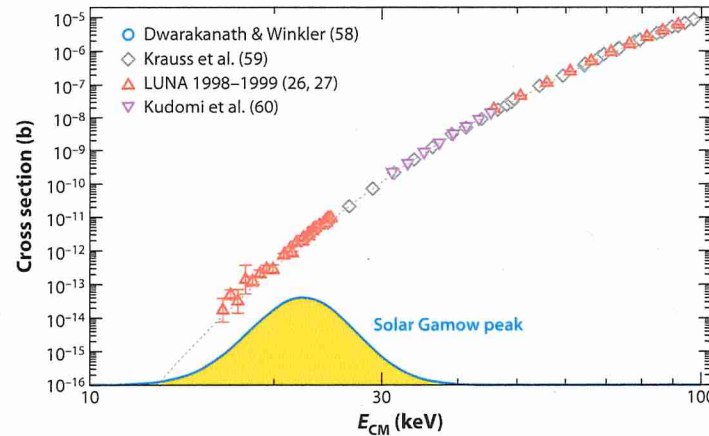



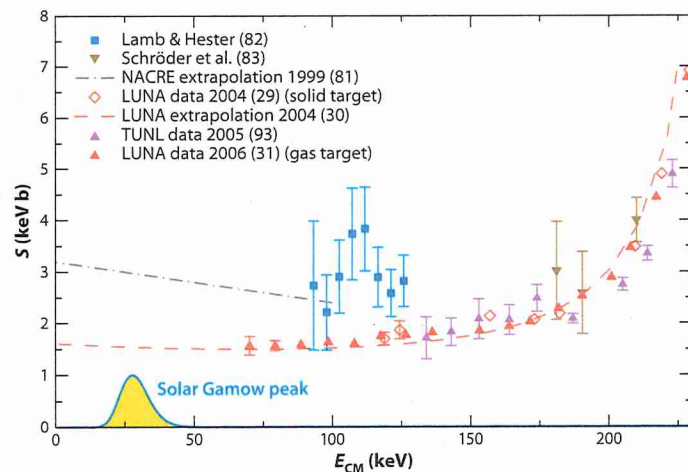
FIG. 3 (color online). The astrophysical S_{12} -factor data sets (Griffiths *et al.*, 1962; Schmid *et al.*, 1996; Ma *et al.*, 1997; Casella *et al.*, 2002) are plotted together with theoretical predictions of Marcucci *et al.* (2005). The solid line represents the “full” theoretical calculation, while the band represents the 68% lower and upper bounds of the adopted quadratic best fit to the four experimental data sets [see text and Eq. (29) for more explanation]. In the inset, the S_{12} factor of the ${}^2\text{H}(p, \gamma){}^3\text{He}$ reaction in the energy range 0–50 keV, obtained with the Argonne v_{18} two-nucleon and Urbana IX three-nucleon Hamiltonian model in the impulse approximation (dashed line) and with inclusion of interaction currents (solid line), is compared with the experimental results.



 Brogini C, et al. 2010.
Annu. Rev. Nucl. Part. Sci. 60:53-73

- A key pp chain reaction in Sun
- Low energy resonance proposed as solar ν solution
— NOT SEEN

Annual Reviews



AR Brogini C, et al. 2010.
Annu. Rev. Nucl. Part. Sci. 60:53–73

- Pace of CNO cycle set by this
- Sets ages of low mass stars

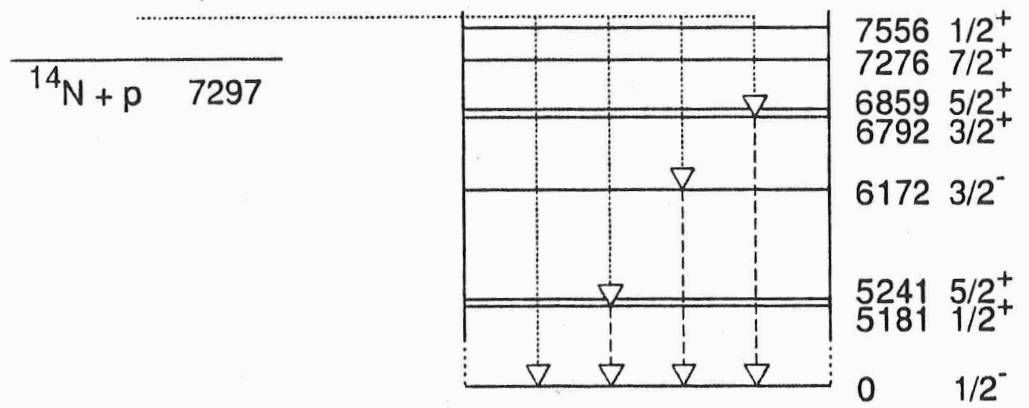


FIG. 1. Energy levels of ^{15}O , in keV [15,21].

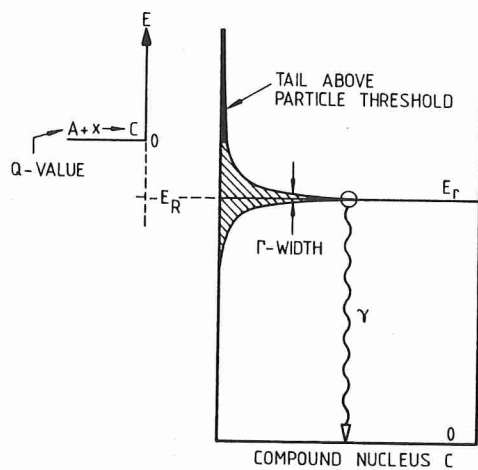


FIGURE 4.16. An excited state of a compound nucleus at an energy E_r , which lies energetically below the particle threshold Q for decay into nuclei A and x . The excited state is shown to decay by γ -ray emission and is characterized by a width Γ . Because of this width Γ , the state E_r extends energetically to both sides of E_r on a rapidly decreasing scale.

SUB-THRESHOLD RESONANCES

SUMMARY

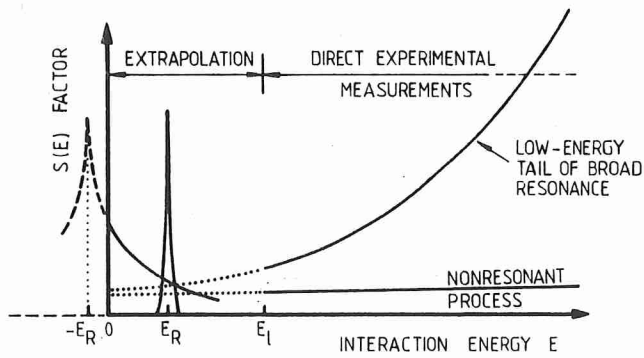


FIGURE 4.18. In charged-particle-induced reactions, the steep drop of the cross section owing to the Coulomb barrier results in a lower limit in energy, E_I , below which direct measurements cannot be carried out. The data are usually presented in the form of the $S(E)$ factor extrapolated to zero energy with the guidance of theory and other arguments. If there is a threshold resonance at $-E_R$ or a resonance only slightly above the particle threshold, the factors can completely dominate the stellar burning. The extrapolated $S(E)$ factor in this case has only a lower limit.

PRIMARYLY for 'light' nuclei reactions
at 'low' temperature as in
H and He-burning

Diavis p203

Eq 3.30

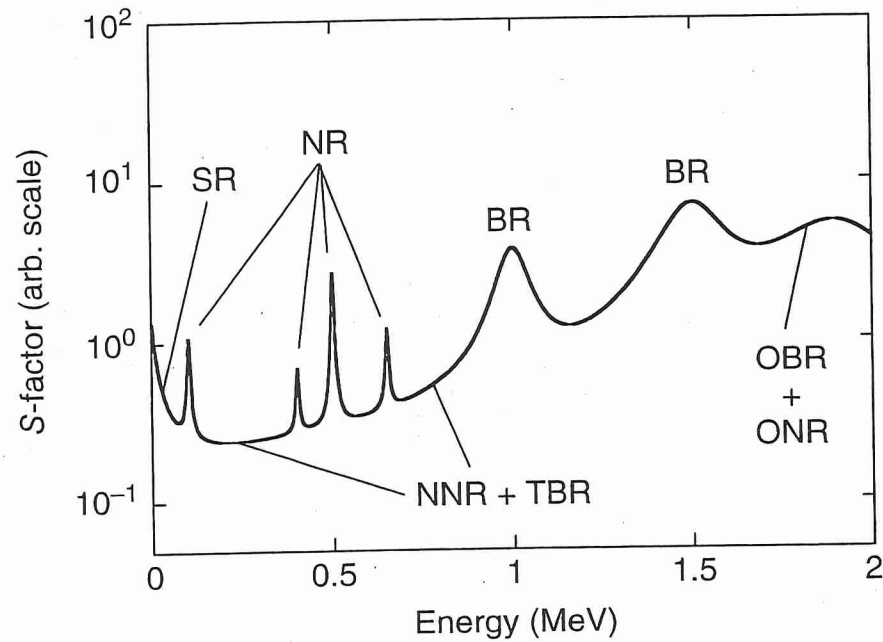


Figure 3.30 Schematic representation of an S -factor versus energy for a charged-particle-induced reaction. At low energies, narrow resonances (NR), wings of subthreshold resonances (SR), tails of broad resonances (TBR), and nonresonant processes (NNR) may

typically contribute to the total S -factor. At higher energies, the S -factor is typically dominated by broad resonances (BR) and by overlapping narrow and broad resonances (OBR + ONR).

COMPOUND NUCLEUS



- C^* has time to share energy among its nucleons

→ INDEPENDENCE HYPOTHESIS

entrance and exit channels decoupled

$$\sigma = \sigma_{\text{formation}}(E) G^c(E)$$

where G is probability of C^* decaying to $B^* + b$

CLASSIC TEST - GOSKAL (1950)

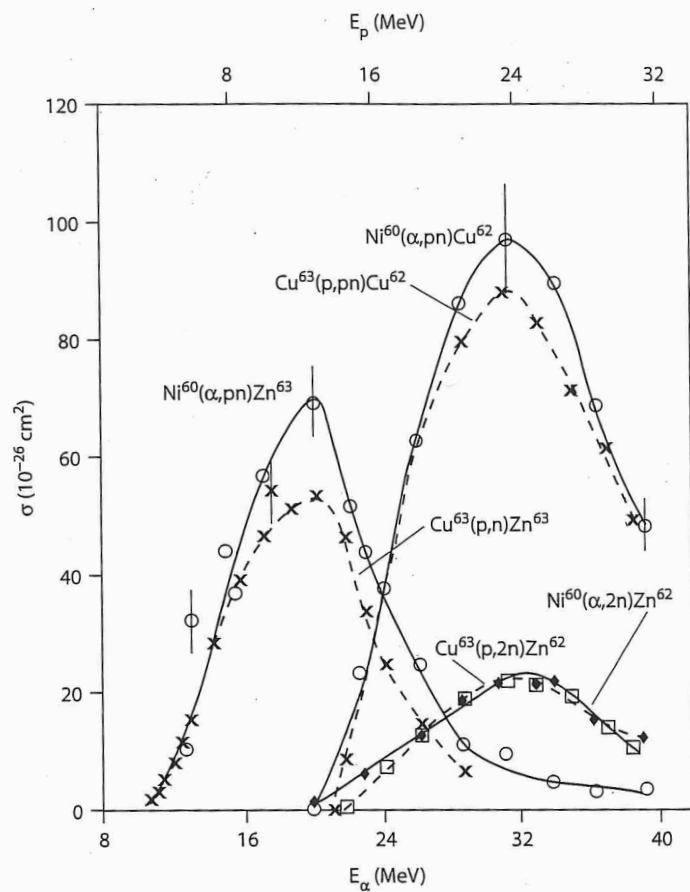


Figure 10.14 Cross sections for the reactions shown in (10.70). The scales of the upper axis (energy of the protons) and lower axis (energy of the α -particle) were adjusted to correspond to the excitation energy of the compound nucleus [Ch50].

HAUSER - FESHBACH STATISTICAL MODEL

- NEED (Iliadis p202)

Nuclear burning - hydrostatic and explosive can involve hundreds to thousands* of reactions involving notably unstable† nuclei

* too many to measure σ 's
† another serious complication

- STATISTICAL theory

- At high energies (as above), number of resonances is high \rightarrow overlapping and to a need for energy-averaged cross-sections

- Basically, an evaporation model calling on compound nucleus and the independence hypothesis

- simple ideas: Cauldrons #432-436

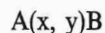
- calculations done for specific
reactors are globally

short-lived radioactive nuclei or nuclei thermally excited to very short-lived excited states. It is sometimes possible to bypass the problem of a radioactive target by inverting the nuclear reaction and then using the principle of time-reversal invariance. Of course, this technique will not work if both target and residual nucleus have short lifetimes (chap. 5), or if excited states are involved in the reaction processes.

Numerous experimental studies show that direct nuclear reactions are rarely significant in the range of nuclei and at the energies that are relevant for astrophysics, and that compound nucleus reactions dominate the processes. The Hauser-Feshbach statistical reaction model (Hau52, Vog68) is therefore usually adequate for a general description of these compound nucleus reactions.

The statistical theory of nuclear reactions (Bla62) is based on the compound nucleus picture of nuclear reactions. The closely spaced narrow resonances, which are characteristic of compound nucleus processes, are individually of interest only at low energies and for the lightest nuclear systems. At higher energies and for the heavier nuclei, the number of resonances increases drastically; the physical interest is in nuclear cross sections averaged over these resonances, which also is usually what is measured. The statistical theory of nuclear reactions deals with such energy-averaged cross sections.

To a large extent, the treatment of average cross sections employs an evaporation model with only a partial basis in nuclear reaction theory. The model depicts the nuclear reaction as proceeding in two stages. In the first stage a compound nucleus is formed by the collision of the projectile with the target nucleus. In the second stage, the compound nucleus decays into one of many possible pairs of reaction products. The evaporation model assumes that the compound nucleus, in its decay, loses all memory of the way in which it was formed. Thus, the decay treats all possible decay products in the democratic fashion envisaged in evaporation of a classical liquid drop. In this evaporation model a nuclear reaction of the type



is assumed to have an energy-averaged cross section $\bar{\sigma}(E)$, which may be factored as

$$\bar{\sigma}(E) = \sigma_{\text{form}}(x + A) \frac{\Gamma(y + B)}{\Gamma_{\text{tot}}}, \quad (8.3)$$

where the average of the cross section is over all the resonances involved. The first factor in the above equation, which depends only on the initial pair of particles in the entrance channel, is called a cross section for the formation of the compound nucleus. The second term represents a branching ratio that describes the probability of decay into the channel of interest, namely, $y + B$, compared with the total decay probability, which is the decay into all pairs of reaction products (exit channels) available to the compound nucleus. This

branching ratio width Γ_{tot} . Clea nucleus only an exit channels. The independent

The cross section be a maximum;

$$\sigma_{\text{form}}(x + A)$$

where the quadratic πR^2 (R is the radius of the nucleus), the particles, the penetration into account by

$$\sigma_{\text{form}}(x + A)$$

For both neutrons and the nuclear doorway states (chap. 4) are well described through the resonance factors. These factors are $T_i(E, R)$. The branching ratio for any channel

$$\bar{\sigma}(E) = \pi \lambda^2$$

If J and π are the resonance states to sum over then

$$\bar{\sigma}(E) = \frac{\pi \lambda^2}{(2j_p + 1)}$$

Here j_t and j_p are the target and projectile spin parities $T_x(J, \pi)$ at the entrance channel and the dissociation of the channel and the

The sum in the above equation is over all the residual nuclei in the entrance channel over orbital angular momentum accessible excitations for which excitation energy is known, the sum is not known. This

branching ratio is proportional to the ratio of partial width $\Gamma(y + B)$ and total width Γ_{tot} . Clearly the total decay probability is a property of the compound nucleus only and does not depend on the particular choice of the entrance and exit channels. The factorization assumed in equation (8.3) is an expression of the independence of formation and decay of the compound nucleus.

The cross section for the formation of the compound nucleus is assumed to be a maximum; that is (chap. 4),

$$\sigma_{\text{form}}(x + A) = \sigma_{\text{max}} = \pi\lambda^2\omega,$$

where the quantity ω is the statistical factor and where for neutrons $\pi\lambda_n^2 = \pi R^2$ (R is the nuclear radius of the colliding pair). In the case of charged particles, the penetration through the Coulomb barrier (chap. 4) must be taken into account by multiplying by the penetration factor $P_l(E, R)$:

$$\sigma_{\text{form}}(x + A) = \pi\lambda^2\omega P_l(E, R).$$

For both neutrons and charged particles, it is assumed that particles reaching the nuclear domain are fully absorbed, i.e., that the reduced particle widths (chap. 4) are unity. This assumption is also applied for the exit channels through the reciprocity theorem. Hence all partial widths $\Gamma(y + B)$ as well as the total width $\Gamma_{\text{tot}} = \sum_i \Gamma_i$ can be replaced by their respective penetration factors. These factors, often called transmission functions, are given by $T_l(E, R)$. The basic Hauser-Feshbach expression for the energy-averaged cross section for any orbital angular momentum l is then

$$\bar{\sigma}(E) = \pi\lambda^2\omega \frac{T_x(l)T_y(l)}{\sum_i T_i(l)}.$$

If J and π are the angular momentum and parity of the compound nucleus resonance states, the reaction can proceed through all such states, and one has to sum over these quantities:

$$\bar{\sigma}(E) = \frac{\pi\lambda^2}{(2j_p + 1)(2j_t + 1)} \sum_{J, \pi} (2J + 1) \frac{T_x(J, \pi)T_y(J, \pi)}{\sum_i T_i(J, \pi)}. \quad (8.4)$$

Here j_t and j_p are the spins of the target nucleus and projectile, and the quantities $T_x(J, \pi)$ and $T_y(J, \pi)$ are the transmission functions for formation and dissociation of the compound nucleus state (J, π) via the $A + x$ entrance channel and the $B + y$ exit channel, respectively.

The sum in the denominator of equation (8.4) includes all states in the residual nuclei that are energetically accessible at the interaction energy E of the entrance channel. Each transmission function contains an implicit sum over orbital angular momentum and channel spin, if applicable. When the accessible excitation energy in the residual nucleus is higher than the energy for which excitation energies, spins, and parities of the excited states are known, the sums will include integrals over the regions where the states are not known. This aspect requires the development of analytic expressions for

(8.3)

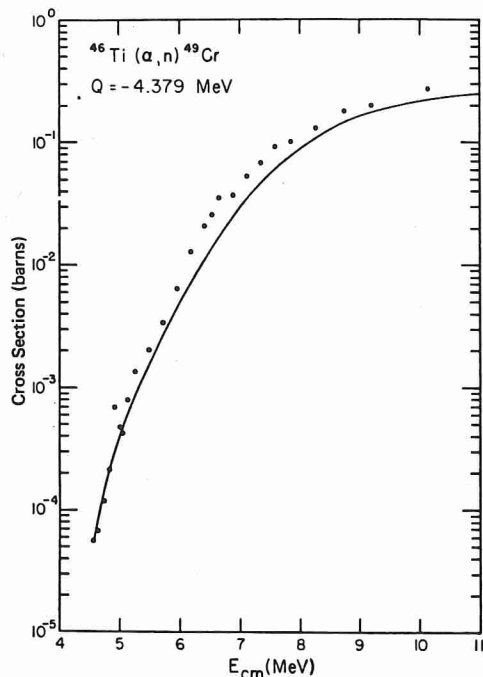


FIGURE 8.8. Comparison of Hauser-Feshbach cross-section calculations with measurements of the $^{46}\text{Ti}(\alpha, n)^{49}\text{Cr}$ reaction (How74). The energy dependence of this reaction cross section is mainly governed by the α -particle transmission functions, except very close to the neutron threshold.

the density of excited states as a function of E , J , and π . The other essential ingredients in the cross-section formula are the transmission functions, which are commonly obtained with the use of optical-model potentials.

Many authors have contributed to the development and improvement of statistical nuclear reaction models (Mic70, Tru66, Tru72, Man75, Hol76, Woo78). This theoretical effort is still going on, and it is possible to hope that a model will be produced that will predict reaction rates to better than a factor of 2. In any case, it is imperative to check, wherever possible, these theoretically predicted reaction rates—in part as an incentive for further improvements in theory. For this reason, there has been considerable experimental effort to measure absolute cross sections, as a function of bombarding energy (so-called excitation functions), for a wide range of silicon-burning nuclear reactions (How74, Rio75). That the Hauser-Feshbach model gives an acceptable description of excitation functions, even with global parameters in the potentials, was quickly verified. Figure 8.8 shows an example. Usually, such excitation functions are rather featureless, and they usually test the energy dependence of only a few of the partial widths, often only that of the entrance

channel. Many of them are measured and reported.

Charged-particle-silicon-burning reactions. These calculations predict the cross sections for these reactions. These calculations are for a given reaction flux is constant, the kind. This situation is another faucet is turned.

The first of these was found (Man75a) in the thresholds for several reactions $^{64}\text{Ni}(p, n)^{64}\text{Cu}$. A factor of 3 smaller than the competition cusps would model than reactions widths must be described program to study such resulting improvements (Bar82).

The current global calculations of reaction cross

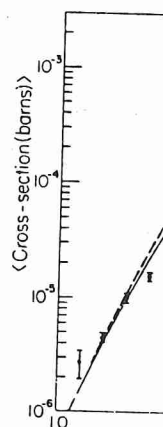


FIGURE 8.9. Competition calculations. The solid (dashed) line (Man75a). Note that, as the solid line is about one-tenth of the maximum

channel. Many of the silicon-burning reactions have not been experimentally measured and represent an open field for future activity in the nuclear laboratory.

Charged-particle-induced cross sections have been calculated for most silicon-burning reactions, with the reaction model as then developed (Woo78). These calculations predict cusplike behavior at neutron thresholds for many reactions. These cusps are seen as relatively sharp drops in the cross section for a given reaction as a second reaction channel opens up. If the incoming flux is constant, there is a reduction in the number of reactions of the first kind. This situation is analogous to the decrease in flow from a water faucet as another faucet is turned on.

The first of these competition cusps, as they are now called (Bar82), was found (Man75a) in the reaction $^{64}\text{Ni}(p, \gamma)^{65}\text{Cu}$ in the energy range where thresholds for several low angular momentum states appear in the competing reaction $^{64}\text{Ni}(p, n)^{64}\text{Cu}$ (Fig. 8.9). The observed competition cusp is about a factor of 3 smaller than predicted. It was immediately recognized that competition cusps would provide a more sensitive test of the nuclear reaction model than reactions without such cusps because all of the significant partial widths must be described correctly to reproduce the observed structure. A program to study such cusps was then undertaken in several laboratories. The resulting improvements on the statistical reaction model are continuing (Bar82).

The current global Hauser-Feshbach models already give acceptable predictions of reaction cross sections for nuclei near the valley of stability. Thiele-

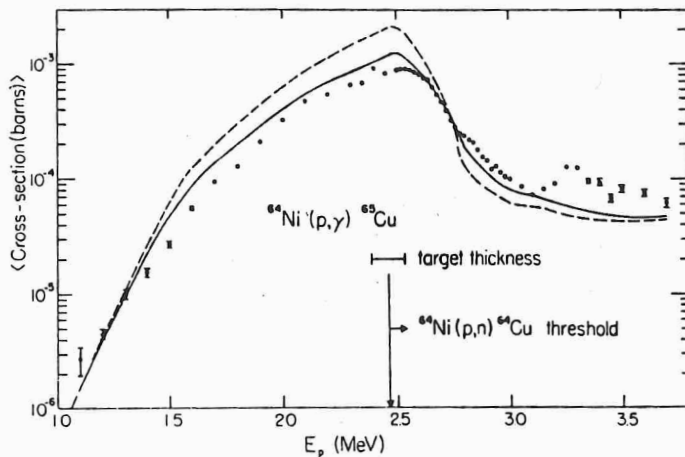


FIGURE 8.9. Competition cusp in $^{64}\text{Ni}(p, \gamma)^{65}\text{Cu}$ compared with the Hauser-Feshbach calculations. The solid (dashed) line is a calculation with (without) width fluctuation corrections (Man75a). Note that, as the successive neutron thresholds open, the (p, γ) yield shows a large drop to about one-tenth of the maximum value reached just below the first neutron threshold.

h measurements of
on cross section is
the neutron thresh-

other essential
functions, which
ls.
improvement of
Man75, Hol76,
ble to hope that
ter than a factor
, these theoretic-
urther improve-
le experimental
nboarding energy
burning nuclear
gives an accept-
arameters in the
le. Usually, such
test the energy
t of the entrance

mann (Thi80) has suggested alternative potentials and level-density expressions, which are claimed to improve the capability of the theory to predict cross sections involving nuclei far from the valley of stable nuclei. At this time, there is no satisfactory way to test experimentally the extrapolation of nuclear reaction models far from the valley of stability, since these nuclei are unstable (chap. 5).

8.3. The Final Bursts of Nucleosynthesis in Massive Stars

We have seen that the silicon core built up in the sequence of quiescent burning phases will eventually contract. The resulting increase in temperature will result in some of the silicon nuclei being broken down into α -particles. These α -particles, in turn, are captured by the rest of the silicon and other nuclei such as sulfur, argon, and calcium, resulting in the formation of iron and nickel. Because of prodigious neutrino losses the energy output of silicon burning is not very large and conversion of the material of the inner region of the star to iron and nickel is rapid. Iron and nickel, the most tightly bound of all nuclei, cannot participate in any reactions providing nuclear energy needed to support the hydrostatic pressure which stabilizes the iron-nickel core and thus prevents gravitational collapse. We have now arrived at a crucial moment in the history of a massive star. We will pause here and examine the existing inner structure of the star (the supernova progenitor) before going on to the inevitable gravitational collapse and the final catastrophic evolutionary event, a giant explosion called a supernova.

8.3.1. The Inner Structure of a Presupernova Star

By the time the iron-nickel core of a massive star forms and the core is just beginning to collapse, the star has gone through many burning stages, and the mantle of the star has evolved into a complex structure, an onion-shell-like composition. The core is surrounded by many distinct layers, each consisting primarily of a specific element. As shown in Figure 8.10, the layers, assuming a star considerably more massive than the sun, and starting at the core, consists of silicon, oxygen, neon, carbon, helium, and hydrogen. The envelope of the star consists of matter similar to that in our sun, i.e., mostly hydrogen. Since temperature and density increase as we go toward the center of the star (Fig. 8.10), the interior boundary of each of these layers is a nuclear-burning zone contributing newly formed heavier matter to the next interior layer. For example, between the hydrogen layer and the helium layer, there is a narrow zone where the temperature is high enough to fuse hydrogen nuclei into helium nuclei. The shells are typically convective but are separated by density gradients sufficiently large to prevent convective mixing between them. From the surface toward the core, such a presupernova structure recapitulates the various evolutionary stages of the star during its quiescent hydrostatic evolution. If these "onion" shells could be ejected into interstellar space, they would

furnish about t
iron. The questi
these shells into

After helium
central core is t
no mass (or on
matter. As a re
interaction betw
energy, cooling
us.

Because the
effect remains
prevent the coi

INN

FIGURE 8.10. Schematic diagram of a massive star prior to its explosion. Each zone has a certain temperature and density, and the layers are separated by density gradients sufficiently large to prevent convective mixing between them. From the surface toward the core, such a presupernova structure recapitulates the various evolutionary stages of the star during its quiescent hydrostatic evolution. If these "onion" shells could be ejected into interstellar space, they would